The Role of Ice Nuclei Recycling in the Maintenance of Cloud Ice in Arctic Mixed-Phase Stratocumulus

Amy Solomon[12], Graham Feingold[2], and Matthew D. Shupe[12]

(1) Cooperative Institute for Research in Environmental Sciences, University of Colorado Boulder, Boulder, Colorado, USA.

(2) Earth System Research Laboratory, National Oceanic and Atmospheric Administration, Boulder, Colorado, USA.

Corresponding author: Amy Solomon, NOAA/ESRL, PSD3, 325 Broadway, Boulder, Colorado 80305-3337, USA. (amy.solomon@noaa.gov)

July 31, 2015

Abstract

This study investigates the maintenance of cloud ice production in Arctic mixed phase stratocumulus in large eddy simulations that include a prognostic ice nuclei (IN) formulation and a diurnal cycle. Balances derived from a mixed-layer model and phase analyses are used to provide insight into buffering mechanisms that maintain ice in these cloud systems. We find that for the case under investigation, IN recycling through subcloud sublimation considerably prolongs ice production over a multi-day integration. This effective source of IN to the cloud dominates over mixing sources from above or below the cloud-driven mixed layer. Competing feedbacks between dynamical mixing and recycling are found to slow the rate of ice lost from the mixed layer when a diurnal cycle is simulated. The results of this study have important implications for maintaining phase partitioning of cloud ice and liquid that determine the radiative forcing of Arctic mixed-phase clouds.

1 Introduction

Reliable climate projections require realistic simulations of Arctic cloud feedbacks. Of particular importance is accurately simulating Arctic mixed-phase stratocumuli (AMPS), which are ubiquitous and play an important role in regional climate due to their impact on the surface energy budget and atmospheric boundary layer structure through cloud-driven turbulence, radiative forcing, and precipitation (Curry et al., 1992; Walsh and Chapman, 1998; Intrieri et al., 2002; Shupe and Intrieri, 2004; Sedlar et al., 2011; Persson, 2012). For example, Bennartz et al. (2012) showed that the extreme melt events observed at Summit, Greenland in July 2012 would not have occurred without the surface radiative forcing produced by AMPS.

AMPS are characterized by a liquid cloud layer with ice crystals that precipitate from cloud base even at temperatures well below freezing (Hobbs and Rangno, 1998; Intrieri et al., 2002; McFarquhar et al., 2007). Radiative cooling near cloud top generates turbulence that maintains the liquid layer and forms an approximately well-mixed layer that extends as far as 500 meters below cloud base. These cloud-driven mixed layers are frequently decoupled from the surface layer, limiting the impact of fluxes of heat, moisture, and aerosols on the cloud layer from below (Solomon et al., 2011; Shupe et al., 2013). However, unlike subtropical cloud-topped boundary layers where decoupling enhances cloud breakup by cutting the cloud system off from the surface source of moisture, decoupled AMPS can persist for extended periods of time due to weak precipitation fluxes out of the mixed layer and relatively moist air entrained into the cloud layer at cloud top (Tjernström et al., 2004; Solomon et al., 2011; Sedlar et al., 2012; Solomon et al., 2014).

AMPS are challenging to model due to uncertainties in ice microphysical processes that determine phase partitioning between ice and radiatively important cloud liquid water (Sandvik et al., 2007; Tjernström et al., 2008; Klein et al., 2009, Karlsson and Svensson, 2011; Barton et al., 2012; Birch et al., 2012; de Boer et al., 2012), which drives turbulence that maintains the system. Phase partitioning depends upon the number, shape, and size of ice crystals, since these determine the efficiency of water vapor uptake by ice and hence the availability of water vapor for droplet formation (Chen and Lamb, 1994; Sheridan et al., 2009; Ervens et al., 2011; Hoose and Möhler, 2012).

Since temperatures in AMPS are too warm for homogenous ice nucleation, ice must form through heterogeneous nucleation. Aerosols with properties to serve as seeds for heterogeneous ice crystal formation are referred to as ice nuclei (IN). A number of different aerosols such as mineral dust (Broadley et al., 2012; Kulkarni et al., 2012; Lüönd et al., 2010; Möhler et al. 2006; Pinti et al., 2012; Welti et al., 2009), soot (DeMott, 1990), sea salts (Wise et al., 2012), and bacteria (Kanji et al., 2011; Levin and Yankofsky, 1983) have been observed to act as IN, all of which nucleate at different temperatures and supersaturation ranges. In addition, observations indicate that nucleation properties are modified by aging and coating of aerosols (Möhler et al., 2005; Cziczo et al. 2009). Heterogeneous ice nucleation can occur by a number of modes: either in the presence of super-cooled droplets, when an aerosol comes into contact with a droplet (contact freezing), is immersed in a droplet (immersion freezing), or by vapor deposition on IN (deposition freezing) (Pruppacher and Klett, 1997).

IN can be entrained into the cloud-driven mixed layer through turbulent mixing from above and/or below. Recent studies indicate that entrainment alone cannot account for observed ice crystal number concentration (N_{ICE}) (Fridlind et al., 2012), motivating the use of diagnostic formulations for ice formation to produce model simulations of AMPS with realistic phase partitioning (Ovchinnikov et al., 2011). While this modeling strategy constrains N_{ICE} to be close to the measured values it eliminates the dynamical-microphysical feedbacks that regulate ice/liquid phase partitioning (Avramov et al., 2011).

Here we investigate a relatively unexplored source of ice production--recycling of ice nuclei in regions of ice subsaturation. AMPS frequently have ice-subsaturated air near the cloud-driven mixed-layer base where falling ice crystals can sublimate, leaving behind IN. This feedback loop is referred to hereon as "recycling". Recycling was found to be significant in large eddy simulations of a single-layer stratocumulus observed during the Department of Energy Atmospheric Radiation Measurement Program's Mixed-Phase Arctic Cloud Experiment (M-PACE; Verlinde et al., 2007; Fan et al., 2009). AMPS observed during M-PACE formed due to a cold-air outbreak, where large fluxes of heat and moisture over the open ocean forced turbulent roll clouds that were coupled to the surface layer. This coupling with the surface layer prevented the identification of the role of dynamics internal to the cloud-driven mixed layer in maintaining phase-partitioning.

In this study we focus on the internal microphysics and dynamics of the cloud-driven mixed layer by investigating processes in an AMPS decoupled from surface sources of moisture, heat, and ice nuclei. We posit that recycling plays a significant role more generally since, for example, assuming an adiabatic vertical profile, a 650 meter-deep mixed layer with a cloud-

top temperature of -16°C requires a water vapor mixing ratio of at least 1.7 g kg^{-1} at mixed-layer base to be saturated with respect to ice, i.e., in order for recycling to be a *negligible* source of ice nuclei in the mixed layer. This value is typically only seen in the Arctic between May-September (Serreze et al., 2012), while persistent AMPS frequently occur outside of these months (Shupe et al., 2011).

We examine the role of IN recycling in maintaining ice production using large eddy simulations of a springtime decoupled AMPS. Three simulations are analyzed; a "Control" with recycling turned on and shortwave radiation turned off (to compare with previous simulations of this case that use different IN formulations and shortwave radiation turned off), "NoRecycle" with IN recycling turned off to identify the impact of recycling on the cloud life-time and phase partitioning, and "SW" with recycling and shortwave radiation turned on to identify the impact of realistic diurnal heating and cooling tendencies on the recycling process. This study builds on previous studies of this case, all of which exclude shortwave radiation (Avramov et al., 2011; Solomon et al., 2011, 2014), by including a prognostic equation for IN and a diurnal cycle. Within this modeling framework we investigate the relative roles of recycling and entrainment of IN in maintaining cloud ice production.

2 Case Description

The case derives from observations of a persistent single-layer Arctic mixed-phase stratocumulus cloud observed near Barrow, AK on 8 April 2008 during the Indirect and Semi-Direct Aerosol Campaign (McFarquhar et al., 2011) (see Fig. 1). The adjacent Beaufort Sea was generally ice covered during this time, with significant areas of open water observed east of Barrow. A 4-K temperature inversion with inversion base at 1.05 km was observed

111 via a radiosonde at 17:34UTC; static stability was near neutral within the mixed layer
112 overlaying a stable near-surface layer with static stability greater than 2 K km^{-1} below 500 m.
113 The water vapor mixing ratio, q_v, decreased from 1.7 g kg^{-1} at the surface to 1.2 g kg^{-1} at
114 cloud top, above which a secondary maximum of 1.6 g kg^{-1} was observed. Winds were east-
115 southeasterly throughout the lowest 2 km.

116 Measurements from ground-based, vertically pointing, 35-GHz cloud radar, micropulse lidar,
117 and dual-channel microwave radiometer at Barrow indicated a mixed-phase cloud layer
118 starting at 8 UTC on 8 April 2008 with a cloud top at approximately 1.5km that slowly
119 descended to approximately 0.5 km over a 26 hour period. At the time of the 17:34 sounding
120 the cloud layer extended into the inversion by 100 m, had a cloud base at 0.9 km, and cloud
121 top at 1.15 km. Cloud ice water path (IWP), derived from cloud radar reflectivity
122 measurements, varied from 20–120 g m^{-2} within 10 min of the sounding, with an uncertainty
123 of up to a factor of 2 (Shupe et al., 2006). Concurrently liquid water path (LWP), derived
124 from dual-channel microwave radiometer measurements, was 39–62 g m^{-2}, with an
125 uncertainty of 20–30 g m^{-2} (Turner et al., 2007).

126 Research flights were conducted by the National Research Council of Canada Convair-580 at
127 22:27-23:00 UTC on 8 April 2008 over the ocean northwest of Barrow (McFarquhar et al.,
128 2011). Droplet concentrations measured by a Particle Measuring Systems Forward Scattering
129 Spectrometer Probe varied between 100 and 200 cm^{-3}. Ice crystal number concentrations
130 measured by Stratton Park Engineering Company 2D-S and Particle Measuring Systems 2D-
131 P optical array probes for sizes larger than 100 μm together averaged 0.4 L^{-1}. IN
132 concentrations measured with the Texas A&M Continuous Flow Diffusion Chamber varied

133 from 0.1 L^{-1} to above 20 L^{-1}. Ice crystal habit estimated using the automated habit
134 classification procedure of Korolev and Sussman (2000) indicated primarily dendritic crystal
135 habits.

136 **3 Model Description**

137 We use the large eddy simulation mode of the Advanced Research WRF model (WRFLES)
138 Version 3.3.1 (Yamaguchi and Feingold, 2012) with the National Center for Atmospheric
139 Research Community Atmospheric Model longwave radiation package (Collins et al., 2004),
140 RRTMG shortwave package (Iacono et al., 2008), the Morrison two-moment microphysical
141 scheme (Morrison et al., 2009), and a 1.5-order turbulent kinetic energy prediction scheme
142 (Skamarock et al., 2008). Surface fluxes are calculated uses the modified MM5 similarity
143 scheme with calculates surface exchange coefficients for heat, moisture, and momentum
144 following Webb (1970) and uses Monin-Obukhov with Carlson-Boland viscous sub-layer
145 and standard similarity functions following Paulson (1970) and Dyer and Hicks (1970).

146 All model runs are initialized with winds, temperature, and water vapor from the 17Z 8 April
147 2008 sounding at Barrow, AK (see Fig.1). Initial surface pressure is 1020 hPa. Divergence is
148 assumed to be $2.5x10^{-6}$ s^{-1} below the temperature inversion and zero above, giving a linear
149 increase in large-scale subsidence from zero at the surface to 2.7 mm s^{-1} at the base of the
150 initial inversion (z=1.1 km). This value for divergence was chosen so that the height of the
151 temperature inversion at cloud top is steady. The divergence used in this study is smaller than
152 the divergence used in the WRFLES study of the same case by Solomon et al. (2014) due to

153 the reduced LWPs in this current study and therefore reduced turbulent entrainment that
154 balances large-scale subsidence in a steady simulation.

155 All simulations are run on a domain of 3.2 × 3.2 × 1.8 km with a horizontal grid spacing of
156 50 m and vertical spacing of 10 m. The domain has 65(x)×65(y)×180(z) gridpoints and is
157 periodic in both the x- and y-directions. The top of the domain is at 1.8 km, which is 0.7 km
158 above cloud top in this case. The model time step is 0.75 s. The structure of the cloud layer is
159 insensitive to changes in resolution and domain size. For example, tests run for Solomon et al.
160 (2014) demonstrated that increasing the vertical and horizontal resolutions by a factor of two
161 resulted in an increase in LWP and IWP by 5% and 1%, respectively, while increasing the
162 domain size by a factor of two in both the x- and y-directions results in an increase in LWP
163 and IWP of less than 1%.

164 Cloud droplets are activated using resolved and subgrid vertical motion (Morrison and Pinto
165 2005) and a log-normal aerosol size distribution (assumed to be ammonium bisulfate and
166 30% insoluble by volume) to derive cloud condensation nuclei spectra following Abdul-
167 Razzak and Ghan (2000). The aerosol accumulation mode is specified with concentrations of
168 165 cm^{-3}, modal diameter of 0.2 μm, and geometric standard deviation of 1.4 μm, based on in
169 situ ISDAC measurements. In this formulation, IN and cloud condensation nuclei are treated
170 as separate species.

171 Temperature and moisture profiles are nudged to the initial profiles in the top 400 m of the
172 domain with a time scale of 1 hour. The model is initialized with winds, temperature, and
173 water vapor similar to the Control integration from Solomon et al. (2014). Horizontal winds

174 are nudged to the initial profiles at and above the initial inversion base with a timescale of 2
175 hours. Initial temperature and subgrid turbulent kinetic energy (TKE) are perturbed below the
176 top of the mixed layer with pseudo-random fluctuations with amplitudes of +/- 0.1 K and 0.1
177 $m^2 s^{-2}$, respectively. The liquid layer is allowed to form in the absence of ice during the first
178 hour of the integration to prevent potential glaciation during spinup.

179 The cloud-driven mixed layer is defined as the region where the liquid-ice water static energy
180 is approximately constant with height. We define the boundaries of the mixed-layer top and
181 base to occur where the slopes of liquid-ice static energy exceed $7x10^{-3}$ K m^{-1} and $1x10^{-3}$ K
182 m^{-1}, respectively. Cloud top and base are defined as the heights where cloud water mixing
183 ratio, q_c, is equal to $1x10^{-4}$ g kg^{-1}.

184 Nested Weather Research and Forecasting (WRF) model simulations of this case performed
185 with an inner grid at LES resolution (Solomon et al. 2011) demonstrate that moisture is
186 provided to the cloud system by a total water inversion at cloud top and that the mixed layer
187 does not extend to the surface, i.e., the mixed layer is largely decoupled from surface sources
188 of moisture. In addition, the nested simulations indicate that cloud liquid water, q_c, is
189 maintained within the temperature inversion by downgradient turbulent fluxes of q_v from
190 above and direct condensation driven by radiative cooling. These processes cause at least
191 20% of q_c to extend into the temperature inversion.

192 WRFLES has been modified to include a prognostic equation for IN number concentration
193 (N_{IN}),

$$\frac{\partial N_{IN}}{\partial t} + ADV + DIFF = \frac{\delta N_{IN}}{\delta t}\Big|_{activation} + \frac{\delta N_{IN}}{\delta t}\Big|_{sublimation} \quad (1)$$

where ADV represents advection and DIFF represents turbulent diffusion. Activation is also referred to as nucleation of ice and sublimation is also referred to as recycling of IN.

Here we adopt an empirical approach by initializing N_{IN} with an observationally based relationship expressing the number of available IN as a function of temperature in regions of water-saturation (DeMott et al., 2010),

$$N_{IN} = \mathrm{F} * 0.117 \exp\big(-0.125 * (\mathrm{T} - 273.2)\big) \quad (2)$$

where F is an empirically derived scale factor and T is temperature in Kelvin. Sixteen prognostic equations are integrated for N_{IN} in equally spaced temperature intervals with nucleation thresholds between -20.2°C and -15.5°C (see Fig. 2). Therefore, additional IN become available for activation as the cloud layer cools. Initial N_{IN} concentrations are a function of the nucleation threshold temperatures and are independent of the in-situ temperature. The in-situ temperature in regions of water saturation determines how many IN are activated. To take deviations from the empirical derivation into account, IN are activated with 50% efficiency (by multiplying the activation tendency in equation (1) by 0.5), however results are insensitive to this parameter (not shown). Due to the pristine dendritic nature of the observed crystals, ice shattering and aggregation are neglected in the simulations and sublimation returns one N_{IN} per crystal.

N_{IN} (in units of L^{-1}) integrated over the domain in each temperature bin k at time t is equal to

$$\overline{N}_{IN}(k,t) = \iiint N_{IN}(x,y,z,k,t)\ dx\ dy\ dz. \qquad (3)$$

Upon sublimation, the modification of activation thresholds that can occur for previously nucleated IN, i.e. preactivation (Roberts and Hallett, 1967), is not considered and N_{IN} are returned to each bin k with weighting

$$\mathrm{W}_k = [\overline{N}_{IN}(k,0) - \overline{N}_{IN}(k,t)\ ]/\ \overline{N}_{IN}(k,0) \qquad (4)$$

where W_k is normalized such that $\sum \mathrm{W}_k = 1$. The W_k are recalculated each time step. In this way, IN are recycled preferentially to each of the 16 temperature bins from which they originated (Feingold et al., 1996).

The factor F in Eq. (2) is set to 4 for all simulations yielding an initial N_{IN} summed over all bins at every gridpoint equal to 5.8 L^{-1}, compared to 10 L^{-1} used in LES studies of the same case presented in Avramov et al. (2011). In a discrete bin formulation this results in 3.26 L^{-1} in the warmest bin and 0.23 L^{-1} additional IN that are available for nucleation in the coldest bin. Given the initial temperatures in the cloud layer, all IN from the first bin in the cloud layer nucleate. This causes an initial spike in cloud ice number concentration, which also causes a large precipitation flux out of the mixed layer. It takes approximately 6 hours for the cloud layer to reach a quasi-equilibrium with steady cloud ice production. Supplementary integrations were done to test for robustness of the results presented in Section 4 by varying initial IN concentrations, i.e., the factor F, (shown in Fig. 3) and by varying snow density and fall speeds (shown in Fig. 4). Fig. 3 shows that the simulation maintains ice production when the initial N_{IN} is increased or decreased by ~3 L^{-1} relative to Control. Fig. 4 shows that the

229 simulations maintain quasi-steady ice and liquid water paths after an initial spinup but the
230 amount of ice produced is sensitive to the snow fall speed.

231 Crystal size distributions for averaged values of ice water mixing ratio and number
232 concentration from the Control integration are shown in Fig. 5. These crystal size
233 distributions are consistent with the Avramov et al. (2011) simulations of this case where
234 crystal habits are assumed to be high-density pristine dendrites. The distribution shown in Fig.
235 5 underestimates the number of large (greater than 5mm) crystals as estimated by the 2D-S
236 and 2D-P probes (see Avramov et al. (2011) for a detailed discussion of the measurements).

237 The Control integration is run with shortwave radiation turned off in order to compare with
238 previous LES studies of this case (Avramov et al. 2011; Solomon et al. 2014). The results of
239 Control are compared to two additional simulations; one with IN recycling turned off
240 (hereafter "NoRecycle") and one with recycling and shortwave radiation both turned on
241 (hereafter "SW"). SW is used to investigate how the diurnal cycle impacts IN recycling and
242 ice formation. All runs use the same setup except SW has subsidence reduced by 30% to
243 keep the mixed-layer top from lowering appreciably because of smaller LWPs. This allows
244 for direct comparisons of mixed layer structure and fluxes at the mixed layer boundaries. The
245 NoRecycle run is started from the Control run at hour 6 to prevent the two simulations from
246 diverging due to spinup. The first six hours of integration are not used in the analysis to allow
247 for the spinup of cloud ice. Hours 6-40 are used for analysis of the Control and NoRecycle
248 simulations and hours 16-76 are used for analysis of the SW simulation to allow for multiple
249 diurnal cycles.

250 **4 Model Results**

4.1 Control Integration

In the quasi-steady Control integration, the mixed-layer depth is approximately 850 m and comprises a 375 m deep mixed-phase cloud layer (henceforth "the cloud layer"), extending above the mixed-layer top by 25 m, and a 500 m subcloud layer below (Fig. 6). IN are produced by sublimation of ice crystals below the cloud layer, advected to the cloud layer by turbulence, and activated as ice crystals (Fig. 6). Ice that forms in the cloud layer is transported vertically by turbulence, precipitates to cloud base and below, and sublimates below the cloud layer. At the mixed-layer base, an increase in N_{ICE} due to precipitation approximately balances a decrease in N_{ICE} due to sublimation. These processes constitute a feedback through which ice production and IN recycling are closely related. This feedback between ice production and IN in the mixed layer is linked to dynamic-thermodynamic tendencies, which sustain a subsaturated subcloud layer because the decrease in relative humidity due to an upward turbulent vapor flux exceeds the increase due to sublimation.

The time evolution of horizontally-averaged IN advection plus subsidence (Fig. 7a) shows that the majority of IN activate at cloud base, which is a bit warmer than cloud top but is sufficiently cold to activate many of the IN. However, IN from bins with colder threshold temperatures are advected higher into the cloud where they activate at their threshold temperature. A secondary maximum is seen at cloud top where the coldest temperatures are found. Also, it is seen that IN are advected into the cloud layer at cloud top for the first 15-18 hours, but this source of IN decreases as IN in the upper entrainment zone are depleted. The turbulent mixing of snow and ice in the mixed-phase cloud layer is clearly seen in Fig. 7b, where ice plus snow number concentrations are well-mixed in the cloud layer. Given the

273 efficient mixing by the turbulent eddies, it is not possible to identify whether ice has
274 nucleated at cloud base or cloud top from the ice number concentrations alone. Fig. 7 also
275 shows the time-height cross sections of horizontally-averaged water vapor mixing ratio and
276 relative humidity with respect to ice. These figures show that the continuous drying and
277 cooling of the mixed layer results in continuous sublimation in the subcloud layer.

278 LWP and IWP remain steady until hour 16 of the simulation, and decrease slowly thereafter
279 (solid lines in Fig. 8a). LWP and IWP magnitudes are within the observational estimates for
280 this case. In addition, the cloud system is sustained over a multi-day period similar to
281 measurements taken during ISDAC. Continuous cloud-top cooling causes the minimum
282 horizontally-averaged temperature (near cloud top) to decrease from -17.5^{o}C to -20^{o}C from
283 hour 10 to hour 40 (Fig. 8b).

284 Over the 40-hour integration, the cloud layer remains decoupled from the surface (Fig. 8c).
285 However, this does not prevent the number concentration of ice crystals (N_{ICE}) in the cloud
286 layer from remaining relatively steady, decreasing from vertically integrated values of 372 to
287 365 m L^{-1} (Fig. 8d, or in terms of vertically averaged cloud layer values, 1.2 L^{-1} to 1.1 L^{-1}).
288 By contrast, while N_{ICE} is maintained in the cloud layer, N_{IN} in the subcloud layer decreases
289 significantly from 2 L^{-1} to 0.2 L^{-1} over the same period. Therefore, even though more N_{ICE}
290 are lost from the cloud than are activated (Fig. 9a), the relatively constant flux of IN into the
291 cloud layer (Fig. 9b) allows N_{ICE} in the cloud to decrease at a slower rate than N_{IN} in the
292 subcloud layer. The continuous loss of N_{IN} in the subcloud layer is due to the IN flux into the
293 cloud layer exceeding the N_{IN} gained through sublimation and turbulent advection at mixed-

294 layer base (Fig. 9b). This loss is not mitigated by entrainment at mixed-layer top, which is
295 found to be negligible (Fig. 9c), consistent with Fridlind et al. (2011).

296 The feedback loops discussed above are illustrated by the conceptual diagram in Fig. 10,
297 where any change to one link in the cycle leads to an increase or decrease in ice production.
298 For example, a decrease in the turbulent advection of N_{IN} into the cloud layer, slows the
299 activation of IN, reduces the precipitation flux into the subcloud layer, reducing sublimation
300 and availability of IN below cloud base. Both dynamics and thermodynamics play a role in
301 the buffering aspect of these feedback loops since, for example, the slowing of IN activation
302 in the example above would lead to increased cloud liquid production, cloud-top radiative
303 cooling, and enhanced turbulent mixing, which would lead to increased transport of IN into
304 the cloud layer and therefore increased activation of IN.

305 ***4.2 Impact of turning off recycling***

306 When IN recycling is turned off, all IN that activate are lost from the system. This results in a
307 more rapid loss of IN, a decrease in IWP, and a rapid increase in LWP (Fig. 8a,d, dashed
308 lines), in contrast to the measurements that show a steady liquid layer and consistent ice
309 production. Increased cloud liquid water when recycling is turned off results in increased
310 radiative cooling at cloud top, which causes the cloud-driven mixed layer to cool more
311 rapidly (Fig. 8b). These results demonstrate the importance of IN recycling in regulating
312 phase partitioning. The rapid increase in LWP increases cloud-generated turbulence via
313 enhanced radiative cooling and increases the turbulent mixing of IN from the subcloud layer
314 into the cloud layer, contributing to a more rapid depletion of IN relative to the Control
315 integration. This process eventually becomes limited due to depletion of IN in the reservoir

316 below (Fig. 9b). Due to the additional activation of IN as the cloud layer cools, ice
317 production is maintained in the absence of recycling and the activation of IN in the cloud
318 layer exceeds the upward IN flux at cloud base (Fig. 9a,b). However, the diminishing N_{IN} in
319 the subcloud layer limits IN activation and N_{ICE} rapidly decreases in the cloud layer (Fig. 8d).

320 ***4.3 Impact of diurnal cycle***

321 A diurnal cycle is added to the Control simulation in order to investigate how the feedback
322 loops identified in the Control and NoRecycle runs are modified with realistic transient
323 heating and cooling tendencies due to variations in incoming shortwave radiation. A question
324 that is addressed in this diurnal simulation is, to what extent is the continuous production of
325 ice in the Control simulation due to the lack of incoming shortwave radiation, which may
326 overestimate the cooling tendencies in the cloud layer, resulting in an overestimate of IN
327 activation? In addition, we investigate whether allowing for a realistic diurnal cycle provides
328 for additional buffering feedbacks.

329 Adding a diurnal cycle to the Control simulation produces a diurnal peak in downwelling
330 surface shortwave radiation of 510 W m^{-2} and 6 hours of total darkness per day (Fig. 11b).
331 As shortwave radiation increases, the net radiative cooling near cloud top diminishes, which
332 decreases cloud-generated turbulence, decreasing LWP and cloud-layer thickness. In addition,
333 it is seen that the peak daily LWP coincides with zero shortwave radiation when in-cloud
334 turbulence and cloud thickness are largest (Fig. 11a). These values are on the low end but
335 within the measurements for this ISDAC case.

Fig. 11a,b shows that LWP and IWP variability is predominantly driven by the diurnal cycle. However, IWP variability is seen to lag LWP by 3-4 hours because as shortwave radiation decreases the cloud layer cools, which increases activation of IN, increasing N_{ICE}, allowing more ice crystals to grow, which increases IWP (Fig. 11a,b). Similar to the Control simulation subcloud N_{IN} decreases at a faster rate than cloud layer N_{ICE}, but allowing for the warming and cooling tendencies in the diurnal cycle results in cloud layer N_{ICE} that decreases 40% more slowly than in the Control simulation (Fig. 11c).

Precipitation and turbulent mixing of N_{ICE} (hereafter turbulent mixing is referred to as "T_{ICE}") at cloud base are out of phase by 10 hours (Fig. 11d), with turbulence leading precipitation. When shortwave radiation is weak or absent, the increase in N_{ICE} eventually becomes limited by a decreasing turbulent mixing of IN ("T_{IN}") into the cloud layer from below, as recycling slows due to a decrease in N_{ICE} flux from the cloud layer (Fig. 11d,f). When shortwave radiation is strong, reduction in IWP is limited by weaker precipitation losses, and attendant weaker sublimation and IN flux into the cloud layer (Fig. 11d,f). Entrainment of N_{IN} at the mixed-layer top is insignificant throughout the integration (Fig. 11e).

5 Analysis from a mixed-layer perspective

The results discussed in Section 4 can be understood from balances in a well-mixed layer with sources/sinks at the upper and lower boundaries. Total particle concentration (N_{IN}+N_{ICE}) is only changed by fluxes at the mixed-layer boundaries when recycling is allowed. These fluxes are entrainment of N_{IN} at mixed-layer top and turbulent mixing of both

357 N_{ICE} and N_{IN} (T_{ICE} and T_{IN}) and precipitation of N_{ICE} (P) at mixed-layer base. Since there
358 are no sources and sinks of N_{IN}+N_{ICE} within the mixed layer, the horizontally-averaged
359 N_{IN}+N_{ICE} flux ($f(z)$) must vary linearly from mixed-layer base to mixed-layer top (Lilly,
360 1968; Bretherton and Wyant, 1997). If it is assumed that f at the mixed-layer base is
361 downward (assumed negative in this formulation) and f at the mixed-layer top is negligible
362 (robust assumptions for a scenario where ice is precipitating from the mixed layer and
363 entrainment is weak), then

$$f(z) = R * \frac{H - z}{H - B}, \qquad B \le z \le H \tag{5}$$

364 where H is the mixed-layer height, B is the mixed-layer base and R is the total N_{IN}+N_{ICE} flux
365 at the mixed-layer base,

$$R = f|_{\text{Mixed-Layer Base}} = [P + T_{ICE} + T_{IN}]_{\text{Mixed-Layer Base}}, \tag{6}$$

366 and

$$[T_{ICE} + T_{IN}]_{\text{Cloud Base}} \approx [f - P]_{\text{Cloud Base}}. \tag{7}$$

367 Since $f < 0$, the turbulent flux of N_{IN} into the cloud layer plus the turbulent flux of N_{ICE} into
368 the subcloud layer is always less than precipitation of N_{ICE} at cloud base. In addition, in a
369 slowly evolving state where $T_{IN}|_{\text{Mixed-Layer Base}} > 0$, total IN flux due to sublimation in the
370 mixed layer, S, can be written as

$$S \approx [P + T_{ICE}]_{\text{Mixed-Layer Base}} - [P + T_{ICE}]_{\text{Cloud Base}} \quad (8a)$$

371 $$\approx [f - T_{IN}]_{\text{Mixed-Layer Base}} - [f - T_{IN}]_{\text{Cloud Base}} \quad (8b)$$

372 and since $f|_{\text{Mixed-Layer Base}}$ is downward and $f|_{\text{Mixed-Layer Top}}$ is negligible (eq. 5),

$$S < T_{IN}|_{\text{Cloud Base}} - T_{IN}|_{\text{Mixed-Layer Base}} \quad (8c)$$

$$< T_{IN}|_{\text{Cloud Base}} . \quad (8d)$$

373 Thus in a well-mixed layer with an upward $T_{IN}|_{\text{Mixed-Layer Base}}$, sublimation is always less than
374 the flux of N_{IN} into the cloud layer.

375 Based on results from Control, precipitation of N_{ICE} at cloud base is sufficient to balance the
376 upward turbulent flux of N_{IN} (i.e., $|T_{IN}| \gg |T_{ICE}|$ at cloud base). Therefore, in a well-mixed
377 layer with precipitation of N_{ICE} at the mixed-layer base that is larger in magnitude than an
378 upward turbulent N_{IN} flux at the mixed-layer base, and assuming negligible entrainment at
379 the mixed-layer top

$$|P|_{\text{Cloud Base}} > T_{IN}|_{\text{Cloud Base}} > S. \quad (9)$$

380 However, if all N_{ICE} sublimate in the mixed layer and the upward turbulent flux of N_{IN}
381 dominates at the mixed-layer base then $f > 0$ and

$$T_{IN}|_{\text{Cloud Base}} > |P|_{\text{Cloud Base}} = S, \quad (10)$$

382 the mixed layer gains $N_{IN}+N_{ICE}$ over time, resulting in a continuously increasing ice
383 production in the cloud layer. In the presence of shortwave radiation (i.e., in the SW
384 simulation), $T_{IN}|_{\text{Cloud Base}}$ is also greater than $|P|_{\text{Cloud Base}}$ after a period of weakened
385 turbulence and weaker precipitation at the mixed-layer base, due to increased activation of
386 N_{IN} due to decreasing shortwave radiation.

387 If IN entrainment at the mixed-layer top is not negligible then $f(z)$ must be modified to
388 include fluxes at the mixed-layer top and $|f|_{\text{Cloud Base}}$ will increase. If $|f|_{\text{Cloud Base}}$ increases
389 such that $f_{\text{Cloud Base}} < P_{\text{Mixed-Layer Base}}$, then sublimation will exceed $T_{IN}|_{\text{Cloud Base}}$.

390 This mixed-layer analysis provides a framework to understand the results presented in
391 Section 4. Specifically, sublimation being less than the turbulent flux of IN is seen to be a
392 property of a well-mixed layer where the total flux at mixed-layer base is downward and the
393 total flux at the mixed-layer top is negligible. In the case where the mixed layer is saturated
394 with respect to ice, sublimation is equal to zero and the turbulent flux of IN at the mixed-
395 layer base is less that the turbulent flux of IN at the cloud base, reducing the flux of IN into
396 the cloud layer. The relationships outlined in this section are appropriate for any AMPS with
397 weak entrainment at cloud top, weak large-scale advective fluxes, and net downward fluxes
398 at the mixed-layer base.

399 **6 Analysis of Buffered Feedbacks in SW**

400 Phase diagrams highlight the processes involved in ice production when a diurnal cycle is
401 allowed (following the arrows from green to blue to black to red in Fig. 12a,b). When
402 incoming shortwave radiation is a maximum, recycling (sublimation) is seen to be at a

403 minimum. This is counterintuitive since subcloud relative humidity is low at this time, which
404 would be expected to produce increased sublimation. However, due to weak turbulent mixing
405 between the cloud and subcloud layers the net N_{ICE} flux into the subcloud layer is weak,
406 resulting in weak sublimation and recycling. This situation is reversed as shortwave radiation
407 decreases, since increased cloud-top cooling increases cloud-driven turbulent mixing, which
408 allows recycling to increase in the regions of reduced subcloud relative humidity. As is seen
409 in the conceptual diagram (Fig. 10), this then leads to an increased N_{ICE} flux into the
410 subcloud layer (green arrows, Fig. 12). However, N_{ICE} in the cloud layer doesn't begin to
411 increase until activation in the cloud layer exceeds the flux of N_{ICE} into the subcloud layer
412 (green arrows). This cycle is further amplified as shortwave radiation decreases, namely,
413 decreased shortwave radiation increases cloud-driven turbulence, increasing the flux of IN
414 into the cloud layer, increasing the activation of IN, which increases N_{ICE} in the cloud layer
415 and the N_{ICE} flux from the cloud layer into the subcloud layer (blue arrows).

416 When incoming shortwave radiation is a minimum, more N_{IN} are activated because the cloud
417 layer cools. However, again we see that N_{ICE} tendencies due to thermodynamics are buffered
418 by the slowing of turbulence-driven feedbacks due to a thickening of the cloud layer. Thus, a
419 net increase in N_{ICE} in the cloud layer, commensurate with an increased IWP and
420 precipitation (black arrows), is buffered by a decrease in the downward turbulent mixing of
421 N_{ICE}, which reduces recycling, slowing the feedback loop (see Fig. 10). During the morning
422 hours, as the cloud layer warms and thins and ice activation becomes less efficient,
423 turbulence continues to decline, slowing the recycling feedback process to the point where
424 limited IN fluxes to the cloud layer inhibit ice production and N_{ICE} declines (red arrows).

7 Summary

We have demonstrated that sustained recycling of IN through a drying subcloud layer and additional activation of N_{IN} due to a cooling cloud layer are sufficient to maintain ice production, and regulate liquid production over multiple days in a decoupled AMPS.

This study provides an idealized framework to understand feedbacks between dynamics and microphysics that maintain phase-partitioning in AMPS. In addition, we have shown that modulation of the cooling of the cloud layer and the humidity of the subcloud layer by the diurnal cycle buffers the mixed-layer system from a loss of particles and promotes the persistence of a mixed-phase cloud system. The results of this study provide insight into the mechanisms and feedbacks that may maintain cloud ice in AMPS even when entrainment of IN at the mixed-layer boundaries is weak. While the balance of these processes changes depending upon the specific conditions of the cloud layer, for example whether the cloud layer is coupled to the surface layer, the mechanisms detailed in this paper will manifest to some degree and therefore the current study provides a framework for understanding the role of recycling in maintaining phase-partitioning in AMPS.

Author Contributions:

A.S., G.F., and M.D.S. conceived and designed the experiments; A.S. performed the simulations; A.S., G.F., and M.D.S. analyzed the model results and co-wrote the paper.

Acknowledgements:

The authors acknowledge discussions with Alex Avramov, Chris Cox, Gijs de Boer, Barbara Ervens, and Ann Fridlind, and Takanobu Yamaguchi for developing the software to run WRF as a large eddy simulation. This research was supported by the Office of Science (BER), U.S. Department of Energy (DE-SC0011918) and the National Science Foundation (ARC-1023366).

449 **References**

450 Abdul-Razzak, H. and Ghan, S. J.: A parameterization of aerosol activation 2. Multiple
451 aerosol types, J. Geophys. Res., 105, 683.–6844, 2000.

452 Avramov, A., Ackerman, A. S., Fridlind, A. M., van Diedenhoven, B., Botta, G., Aydin, K.,
453 Verlinde, J., Korolev, A. V., Strapp, J. W., McFarquhar, G. M., Jackson, R., Brooks, S.
454 D., Glen, A., and Wolde, M.: Toward ice formation closure in Arctic mixed-phase
455 boundary layer clouds during ISDAC, J. Geophys. Res., 116, D00T08,
456 doi:10.1029/2011JD015910, 2011.

457 Barton, N. P., Klein, S. A., Boyle, J. S., and Zhang, Y. Y.: Arctic synoptic regimes:
458 Comparing domain wide Arctic cloud observations with CAM4 and CAM5 during
459 similar dynamics, J. Geophys. Res., 117, D15205, doi:10.1029/2012JD017589, 2012.

460 Bennartz, R., Shupe, M., Turner, D., Walden, V., Steffen, K., Cox, C., Kulie, M. S., Miller,
461 N., and Pettersen, C.: July 2012 Greenland melt extent enhanced by low-level liquid
462 clouds, Nature, 496, 83-86, doi:10.1038/nature12002, 2012.

463 Birch, C. E., Brooks, I. M., Tjernström, M., Shupe, M. D., Mauritsen, T., Sedlar, J., Lock, A.
464 P., Earnshaw, P., Persson, P. O. G., Milton, S. F., and Leck, C.: Modeling atmospheric
465 structure, cloud and their response to CCN in the central Arctic: ASCOS case studies,
466 Atmos. Chem. Phys., 12, 3419-3435, doi:10.5194/acp-12-3419-2012, 2012.

467 Bretherton, C. S. and Wyant, M. C.: Moisture transport, lower-tropospheric stability, and
468 decoupling of cloud-topped boundary layers, J. Atmos. Sci., 54, 148-167, 1997.

469 Broadley, S., Murray, B., Herbert, R., Atkinson, J., Dobbie, S., Malkin, T., Condliffe, E., and
470 Neve, L.: Immersion mode heterogeneous ice nucleation by an illite rich powder
471 representative of atmospheric mineral dust, Atmos. Chem. Phys., 12:287{307,

doi:10.5194/acp-12-287-2012, 2012.

Chen, J.-P. and Lamb, D.: The theoretical basis for the parameterization of ice crystal habits: Growth by vapor deposition, J. Atmos. Sci., 51, 1206–1222, doi:10.1175/1520-0469(1994)051<1206:TTBFTP>2.0.CO;2, 1994.

Collins, W. D., Rasch, P. J., Boville, B. A., Hack, J. J., McCaa, J. R., Williamson, D. L., and Briegleb, B. P.: Description of the NCAR Community Atmosphere Model (CAM 3.0), NCAR Technical Note, NCAR/TN-464+STR, 226 pp., 2004.

Curry, J. and Ebert, E. E.: Annual cycle of radiation fluxes over the Arctic Ocean: Sensitivity to cloud optical properties, J. Climate, 5, 1267–1280, 1992.

Cziczo, D., Froyd, K., Gallavardin, S., Moehler, O., Benz, S., Saatho, H., and Murphy, D.: Deactivation of ice nuclei due to atmospherically relevant surface coatings, Environ. Res. Lett., 4:044013, doi:10.1088/1748-9326/4/4/044013, 2009.

de Boer, G., Chapman, W., Kay, J. E., Medeiros, B., Shupe, M. D., Vavrus, S., and Walsh, J.: A characterization of the present-day Arctic atmosphere in CCSM4, J. Climate, 25, 2676–2695, 2012.

DeMott, P. J.: An exploratory study of ice nucleation by soot aerosols, J. Appl. Meteorol., 29(10), 1072–1079, 1990.

DeMott, P. J., Prenni, A. J., Liu, X., Petters, M. D., Twohy, C. H., Richardson, M. S., Eidhammer, T., Kreidenweis, S. M., and Rogers, D. C.: Predicting global atmospheric ice nuclei distributions and their impacts on climate, P. Natl. Acad. Sci. USA, 107, 11217-11222, doi:10.1073/pnas.0910818107, 2010.

Dyer, A. J. and Hicks, B. B.: Flux-gradient relationships in the constant flux layer, Q. J. Roy. Meteor. Soc., 96, 715–721, 1970.

Ervens, B., Feingold, G., Sulia, K., and Harrington, J.: The impact of microphysical parameters, ice nucleation mode, and habit growth on the ice/liquid partitioning in mixed-phase Arctic clouds, J. Geophys. Res., 116, D17205, doi:10.1029/2011JD015729, 2011.

Fan, J., Ovchinnikov, M., Comstock, J. M., McFarlane, S. A., and Khain, A.: Ice formation in Arctic mixed-phase clouds: Insights from a 3-D cloud-resolving model with size-resolved aerosol and cloud microphysics, J. Geophys. Res., 114, D04205, doi:10.1029/2008JD010782, 2009.

Feingold, G., Kreidenweis, S. M., Stevens, B., and Cotton, W. R.: Numerical simulation of stratocumulus processing of cloud condensation nuclei through collision-coalescence, J. Geophys. Res., 101, 21,391-21,402, 1996.

Fridlind, A. M., van Diedenhoven, B., Ackerman, A. S., Avramov, A., Mrowiec, A., Morrison, H., Zuidema, P., and Shupe, M. D.: A FIRE-ACE/SHEBA case study of mixed-phase Arctic boundary-layer clouds: Entrainment rate limitations on rapid primary ice nucleation processes, J. Atmos. Sci., 69, 365-389, doi:10.1175/JAS-D-11-052.1, 2012.

Hobbs, P. V. and Rangno A. L.: Microstructure of low and middle- level clouds over the Beaufort Sea, Q. J. Roy. Meteor. Soc., 124, 2035-2071, 1998.

Hoose, C. and Möhler, O.: Heterogeneous ice nucleation on atmospheric aerosols: a review of results from laboratory experiments, Atmos. Chem. Phys., 12, 9817-9854, doi:10.5194/acp-12-9817-2012, 2012.

Iacono, M. J., Delamere, J. S., Mlawer, E. J., Shephard, M. W., Clough, S. A., and Collins, W. D.: Radiative forcing by long-lived greenhouse gases: Calculations with the AER

518 Radiative transfer models, J. Geophys. Res., 113, D13103, doi:10.1029/2008JD009944,
519 2008.
520 Intrieri, J. M., Fairall, C. W., Shupe, M. D., Persson, P. O. G., Andreas, E., Guest, P. S., and
521 Moritz, R. E.: An annual cycle of Arctic surface cloud forcing at SHEBA, J. Geophys.
522 Res., 107, 8039, doi:10.1029/2000JC000439, 2002.
523 Kanji, Z., DeMott, P., Möhler, O., and Abbatt, J.: Results from the University of Toronto
524 continuous flow diffusion chamber at ICIS 2007: instrument intercomparison and ice
525 onsets for different aerosol types, Atmos. Chem. Phys., 11:31-41, doi:10.5194/acp-11-
526 31-2011, 2011.
527 Karlsson, J. and Svensson, G.: The simulation of Arctic clouds and their influence on the
528 winter surface temperature in present-day climate in the CMIP3 multi-model dataset,
529 Clim. Dynam., 36, 623–635, 2011.
530 Klein, S. A., McCoy, R., Morrison, H., Ackerman, A., Avramov, A., de Boer, G., Chen, M.,
531 Cole, J., DelGenio, A. D., Falk, M., Foster, M., Fridlind, A., Golaz, J.-C., Hashino, T.,
532 Harrington, J., Hoose, C., Khairoutdinov, M., Larson, V., Liu, X., Luo, Y., McFarquhar,
533 G., Menon, S., Neggers, R., Park, S., von Salzen, K., Schmidt, J. M., Sednev, I.,
534 Shipway, B., Shupe, M., Spangenberg, D., Sud, Y., Turner, D., Veron, D., Walker, G.,
535 Wang, Z., Wolf, A., Xie, S., Xu, K.-M., Yang, G., and Zhang, G.: Intercomparison of
536 model simulations of mixed-phase clouds observed during the ARM Mixed-Phase Arctic
537 Cloud Experiment. I: Single-layer cloud, Q. J. Roy. Meteor. Soc., 135, 979–1002, 2009.
538 Korolev, A.: Limitations of the Wegener–Bergeron–Findeisen mechanism in the evolution of
539 mixed-phase clouds, J. Atmos. Sci., 64, 3372–3375, doi:10.1175/JAS4035.1, 2007.

Korolev, A. and Sussman, B.: A technique for habit classification of cloud particles, J. Atmos. Oceanic Technol., 17, 1048–1057, 2000.

Kulkarni, G., Fan, J., Comstock, J., Liu, X., and Ovchinnikov, M.: Laboratory measurements and model sensitivity studies of dust deposition ice nucleation, Atmos. Chem. Phys., 12:7295-7308, doi:10.5194/acp-12-7295-2012, 2012.

Levin, Z. and Yankofsky, S.: Contact versus immersion freezing of freely suspended droplets by bacterial ice nuclei, J. Appl. Meteorol. Clim., 22, 1964-1966, 1983.

Lilly, D. K.: Models of cloud-topped mixed layers under a strong inversion, Q. J. Roy. Meteor. Soc., 94, 292–309, 1968.

Lüönd, F., Stetzer, O., Welti, A., and Lohmann, U.: Experimental study on ice nucleation ability of size selected kaolinite particles in the immersion mode, J. Geophys. Res., 115:D14201, doi:10.1029/2009JD012959, 2010.

McFarquhar, G. M., Zhang, G., Poellot, M. R., Kok, G. L., McCoy, R., Tooman, T., Fridlind, A., and Heymsfield, A. J.: Ice properties of single-layer stratocumulus during the Mixed-Phase Arctic Cloud Experiment: 1. Observations, J. Geophys. Res., 112, D24201, doi:10.1029/2007JD008633, 2007.

McFarquhar, G. M., Ghan, S., Verlinde, J., Korolev, A., Strapp, J. W., Schmid, B., Tomlinson, J. M., Wolde, M., Brooks, S. D., Cziczo, D., Dubey, M. K., Fan, J., Flynn, C., Gultepe, I., Hubbe, J., Gilles, M. K., Laskin, A., Lawson, P., Leaitch, W. R., Liu, P., Liu, X., Lubin, D., Mazzoleni, C., Macdonald, A.-M., Moffet, R. C., Morrison, H., Ovchinnikov, M., Shupe, M. D., Turner, D. D., Xie, S., Zelenyuk, A., Bae, K., Freer, M., and Glen, A.: Indirect and Semi-Direct Aerosol Campaign (ISDAC): The Impact of

562 Arctic Aerosols on Clouds, B. Am. Meteorol. Soc., 92, 183–201,
563 doi:10.1175/2010BAMS2935.1, 2011.
564 Möhler, O., Bütuner, S., Linke, C., Schnaiter, M., Saathoff, H., Stetzer, O., Wagner, R.,
565 Krämer, M., Mangold, A., Ebert, V., and Schurath, U.: Effect of sulfuric acid coating on
566 heterogeneous ice nucleation by soot aerosol particles, J. Geophys. Res., 110:D11210,
567 doi: 10.1029/2004JD005169, 2005.
568 Möhler, O., Field, P., Connolly, P., Benz, S., Saathoff, H., Schnaiter, M., Wagner, R., Cotton,
569 R., Krämer, M., Mangold, A., and Heymsfield, A.: Efficiency of the deposition mode ice
570 nucleation on mineral dust particles, Atmos. Chem. Phys., 6:3007-3021,
571 doi:10.5194/acp-6-3007-2006, 2006.
572 Morrison, H. and Pinto, J. O.: Mesoscale modeling of springtime Arctic mixed-phase
573 stratiform clouds using a new two-moment bulk microphysics scheme, J. Atmos. Sci., 62,
574 3683-3704, 2005.
575 Morrison, H., Thompson, G., and Tatarskii, V.: Impact of cloud microphysics on the
576 development of trailing stratiform precipitation in a simulated squall line: Comparison of
577 one- and two-moment schemes, Mon. Wea. Rev., 137, 991-1007,
578 doi:10.1175/2008MWR2556.1, 2009.
579 Paulson, C. A.: The mathematical representation of wind speed and temperature profiles in
580 the unstable atmospheric surface layer, J. Appl. Meteor., 9, 857–861, 1970.
581 Persson, P. O. G.: Onset and end of the summer melt season over sea ice: Thermal structure
582 and surface energy perspective from SHEBA, Clim. Dynam., 39, 1349-1371,
583 doi:10.1007/s00382-011-1196-9, 2012.

584 Pinti, V., Marcolli, C., Zobrist, B., Hoyle, C., and Peter, T.: Ice nucleation efficiency of clay
585 minerals in the immersion mode, Atmos. Chem. Phys., 12:5859-5878, doi:10.5194/acp-
586 12-5859-2012, 2012.
587 Pruppacher, H. and Klett, J.: Microphysics of clouds and precipitation. Kluwer Academic
588 Publishers, 2nd edition, 1997.
589 Roberts, P. and Hallett, J.: A laboratory study of the ice nucleating properties of some
590 mineral particulates, Q. J. R. Meteorol. Soc., 94, 25 – 34, 1967.
591 Sandvik, A., Biryulina, M., Kvamsto, N., Stamnes, J., and Stamnes, K.: Observed and
592 simulated microphysical composition of Arctic clouds: Data properties and model
593 validation, J. Geophys. Res. 112, D05205, 2007.
594 Sedlar, J., Shupe, M. D., and Tjernström, M.: On the relationship between thermodynamic
595 structure, cloud top, and climate significance in the Arctic, J. Climate, 25, 2374–2393,
596 2012.
597 Sedlar, J., Tjernström, M., Mauritsen, T., Shupe, M. D., Brooks, I. M., Persson, P. O. G.,
598 Birch, C. E., and C. Leck, C.: A transitioning Arctic surface energy budget: The impacts
599 of solar zenith angle, surface albedo and cloud radiative forcing, Clim. Dynam., 37,
600 1643–1660, doi:10.1007/s00382-010-0937-5, 2011.
601 Serreze, M. C., Barrett, A. P., and Stroeve, J.: Recent changes in tropospheric water vapor
602 over the Arctic as assessed from radiosondes and atmospheric reanalyses. J. Geophys.
603 Res., 117, D10104, doi:10.1029/2011JD017421, 2012.
604 Sheridan, L. M., Harrington, J. Y., Lamb, D., and Sulia, K.: Influence of ice crystal aspect
605 ratio on the evolution of ice size spectra during vapor depositional growth, J. Atmos. Sci.,
606 66, 3732–3743, doi:10.1175/2009JAS3113.1, 2009.

607 Shupe, M. D.: A ground-based multiple remote-sensor cloud phase classifier, Geophys. Res.
608 Lett., 34, L2209, doi:10.1029/2007GL031008, 2007.
609 Shupe, M. D and J. M. Intrieri: Cloud radiative forcing of the Arctic surface: The influence
610 of cloud properties, surface albedo, and solar zenith angle, J. Climate, 17, 616-628, 2004.
611 Shupe, M. D, Matrosov, S. Y., and Uttal, T.: Arctic mixed phase cloud properties derived
612 from surface-based sensors at SHEBA, J. Atmos. Sci., 63, 697-811, 2006.
613 Shupe, M. D, Persson, P. O. G., Brooks, I. M., Tjernström, M., Sedlar, J., Mauritsen, T.,
614 Sjogren, S., and Leck, C.: Cloud and boundary layer interactions over the Arctic sea-ice
615 in late summer, Atmos. Chem. Phys., 13, 9379-9400, 2013.
616 Skamarock, W. C., Klemp, J. B., Dudhia, J., Gill, D. O., Barker, D. M., Duda, M. G., Huang,
617 X.-Y., Wang, W., and Powers, J. G.: A description of the Advanced Research WRF
618 version 3, NCAR Tech. Note NCAR/TN-475+STR, 113 pp., 2008.
619 Solomon, A., Morrison, H., Persson, P. O. G., Shupe, M. D., and Bao, J.-W.: Investigation of
620 microphysical parameterizations of snow and ice in Arctic clouds during M-PACE
621 through model-observation comparisons, Mon. Wea. Rev., 137, 3110-3128,
622 doi:10.1175/2009MWR2688.1, 2009.
623 Solomon, A., Shupe, M. D., Persson, P. O. G., and Morrison, H.: Moisture and dynamical
624 interactions maintaining decoupled Arctic mixed-phase stratocumulus in the presence of
625 a humidity inversion, Atmos. Chem. Phys, 11, 10127-10148, doi:10.5194/acp-11-10127-
626 2011, 2011.
627 Solomon, A., Shupe, M. D., Persson, P. O. G., Morrison, H., Yamaguchi, T., Caldwell, P. M.,
628 and de Boer, G.: The sensitivity of springtime Arctic mixed-phase stratocumulus clouds

629 to surface layer and cloud-top inversion layer moisture sources, J. Atmos. Sci., 71, 574-
630 595, doi:10.1175/JAS-D-13-0179.1, 2014.
631 Tjernström, M., Sedlar, J., and Shupe, M. D.: How well do regional climate models
632 reproduce radiation and clouds in the Arctic? An evaluation of ARCMIP simulations, J.
633 Appl. Met. Clim., 47, 2405–2422, 2008.
634 Tjernström, M., C. Leck, C., Persson, P. O. G., Jensen, M. L., Oncley, S. P., and Targino, A.:
635 The summertime Arctic atmosphere: Meteorological measurements during the Arctic
636 Ocean Experiment 2001, B. Am. Meteorol. Soc., 85, 1305–1321, 2004.
637 Turner, D. D., Clough, S. A., Liljegren, J. C., Clothiaux, E. E., Cady-Pereira, K., and Gaustad,
638 K. L.: Retrieving precipitable water vapor and liquid water path from Atmospheric
639 Radiation Measurement (ARM) program's microwave radiometers, IEEE T. Geosci.
640 Remote, 45, 3680–3690, 2007.
641 Verlinde, J., Harrington, J. Y., McFarquhar, G. M., et al.: The Mixed-Phase Arctic Cloud
642 Experiment (M-PACE), B. Am. Meteorol. Soc., 88, 205–221, doi:10.1175/BAMS-88-2-
643 205, 2007.
644 Walsh, J. E. and Chapman, W. L.: Arctic cloud-radiation temperature associations in
645 observational data and atmospheric reanalyses, J. Climate, 11, 3030–3045, 1998.
646 Webb, E. K.: Profile relationships: The log-linear range, and extension to strong stability.
647 Quart. J. Roy. Meteor. Soc., 96, 67–90, 1970.
648 Wise, M., Baustian, K., Koop, T., Freedman, M., Jensen, E., and Tolbert, M.: Depositional
649 ice nucleation onto crystalline hydrated nacl particles: a new mechanism for ice
650 formation in the troposphere, Atmos. Chem. Phys., 12:1121-1134, doi:10.5194/acp-12-
651 1121-2012, 2012.

652 Yamaguchi, T. and Feingold, G.: Technical note: Large-eddy simulation of cloudy boundary
653 layer with the Advanced Research WRF model, J. Adv. Model. Earth Syst., 4, M09003,
654 doi:10.1029/2012MS000164, 2012.

655 **Figure Captions**

656 **Figure 1:** Sounding measured at 17:34 UTC 8 April 2008 at Barrow, Alaska (71.338N,
657 156.68W). Left) Water vapor mixing ratio (q_v), temperature (T), and potential temperature
658 (Theta), in units of g kg^{-1}, degrees Kelvin, and degrees Kelvin respectively. Right) Zonal
659 wind (U) and meridional wind (V), in units of m s^{-1}. Gray shading marks the extent of the
660 cloud layer. The dashed lines show the initial profiles used in the WRFLES experiments. The
661 dashed line overlaying water vapor mixing ratio is the initial profile for the total water
662 mixing ratio.

663 **Figure 2:** IN number concentration active at water saturation vs. temperature based on the
664 empirical relationship derived in DeMott et al. (2010) (blue line) used to initialize IN number
665 concentration in each bin. Black vertical lines indicate threshold temperatures for nucleation
666 in the 16 IN bins. IN increments between lines indicate the additional IN available for
667 nucleation at colder temperatures.

668 **Figure 3:** Sensitivity of ice water path to the parameter F in equation (2). Note the similar ice
669 water paths for F=4 and F=6 (total N_{IN} initial values 5.8 and 8.7 L^{-1}, respectively).

670 **Figure 4:** A,B,D) Sensitivity of LWP and IWP to snow density and fall speeds. LWP shown
671 with solid lines and IWP shown with dashed lines, in units of g m^{-2}. C) Fall speeds used in
672 sensitivity studies, in units of m s^{-1}. A) Sensitivity to reducing snow density from 100 kg m^{-3}
673 to 50 kg m^{-3} (red lines) using Control (CNT) fall speeds (red line in C). B) Sensitivity to
674 reducing snow fall speeds (green line in C) using Control snow density (red lines). D)
675 Sensitivity to increasing snow fall speeds (blue line in C) using Control snow density (red
676 lines).

677 **Figure 5:** Simulated ice particle number size distributions using in-cloud mass and number
678 concentrations. Ice water mixing ratio = 3e-4 g/kg, ice number concentration = 0.4/L, snow
679 water mixing ratio = 2.4e-2 g/kg, snow number concentration = 0.45/L.

680 **Figure 6:** (A) N_{IN} and (B) N_{ICE} averaged over 0.5 hours at hour 20, in units of L^{-1} hr^{-1}. Grey
681 shading indicates the extent of the cloud layer. Green dash lines indicate the top and bottom
682 of the mixed layer.

683 **Figure 7:** Time-height cross sections of horizontally-averaged (A) IN advection plus
684 subsidence, in units of $L^{-1}hour^{-1}$, (B) ice plus snow number concentration, in units of L^{-1}, (C)
685 water vapor mixing ratio, in units of g kg^{-1}, and (D) relative humidity with respect to ice, in
686 units of percent, from CNT simulation. Temperature, in units of °C, shown with black
687 contour lines in (B,C,D).

688 **Figure 8:** Control and NoRecycle time series for hours 6-40 (smoothed with 90 minute
689 running average). NoRecycle shown with red and black dashed lines. A) LWP (black) and
690 IWP (red), in units of g m^{-2}. B) Minimum horizontally-averaged temperature in the column,
691 in units of ^{o}C. C) Mixed-layer depth (blue), top height (red), and base height (black), in units
692 of km. D) N_{ICE} integrated over cloud layer (referred to as CL, red) and N_{IN} integrated over
693 subcloud layer (referred to as SubCL, black), in units of m L^{-1}(i.e., meters/liter).

694 **Figure 9:** Horizontally-averaged fluxes from Control and NoRecycle integrations for hours
695 6-40 (smoothed with 90 minute running average). NoRecycle shown with red and black
696 dashed lines. A) N_{ICE} flux at cloud base due to turbulence+subsidence+precipitation (red),
697 mixed-layer base due to turbulence+subsidence+precipitation (black), and due to activation
698 (multiplied by -1, blue), in units of m L^{-1} hr^{-1}. B) N_{IN} flux at cloud base due to turbulence

699 (red), N_{IN} flux due to sublimation (black), and precipitation of N_{ICE} at cloud base (multiplied
700 by -1, blue), in units of m L^{-1} hr^{-1}. C) N_{IN} entrainment at mixed-layer top (red) and base
701 (black), in units of m L^{-1} hr^{-1}.

702 **Figure 10:** Schematic of feedback loops that maintain ice production and the phase-
703 partitioning between cloud liquid and ice in an AMPS. Red colors denote N_{IN}. Blue colors
704 denote N_{ICE}. The size of the arrow indicates the relative magnitude of the flux. Vertical
705 profiles of N_{ICE}, N_{IN}, relative humidity, and temperature shown with thin blue, red, green, and
706 yellow lines, respectively.

707 **Figure 11:** A) LWP (black) and IWP (red), in units of g m^{-2}. (B) Downward surface
708 shortwave radiation and turbulent kinetic energy (TKE) at cloud base, in units of Wm^{-2} and
709 m^2s^{-2}, respectively. C) N_{ICE} in cloud layer (referred to as CL, red) and N_{IN} in subcloud layer
710 (referred to as SubCL, black), in units of m L^{-1}. (D) Total, turbulent, precipitation N_{ICE} flux at
711 cloud base (referred to as CL base, red, green, blue, respectively) and total N_{ICE} flux at
712 mixed-layer base (referred to as ML base, black), in units of m L^{-1} hr^{-1}, for the SW
713 integration for hours 16-76. Grey shading indicates hours with zero downwelling surface
714 shortwave radiation. E) N_{IN} entrainment at mixed-layer top (red) and base (black), in units of
715 m L^{-1} hr^{-1}. (F) N_{IN} flux at cloud base due to turbulence (red), N_{IN} flux due to sublimation
716 (black), and activation of N_{ICE} (blue), in units of m L^{-1} hr^{-1}.

717 **Figure 12:** A) Phase diagram of TKE at cloud base vs. N_{ICE} in the cloud layer starting at
718 peak shortwave hour 40, in units of m L^{-1} and m L^{-1} hr^{-1}, respectively. Colors show
719 sublimation in units of m L^{-1} hr^{-1}. H) 24-hour phase diagrams of sublimation vs. minimum
720 relative humidity in the subcloud layer starting at peak shortwave hour 40, in units of m L^{-1}

721 hr^{-1} and %, respectively. Colors show total N_{ICE} flux at cloud base, m L^{-1} hr^{-1}. Hours 42-47,
722 47-50, 50-56, and 57-62 indicated with green, blue, black, red arrows, respectively.
723 Minimum shortwave indicated with the moon symbol. Maximum shortwave indicated with
724 the sun symbol.

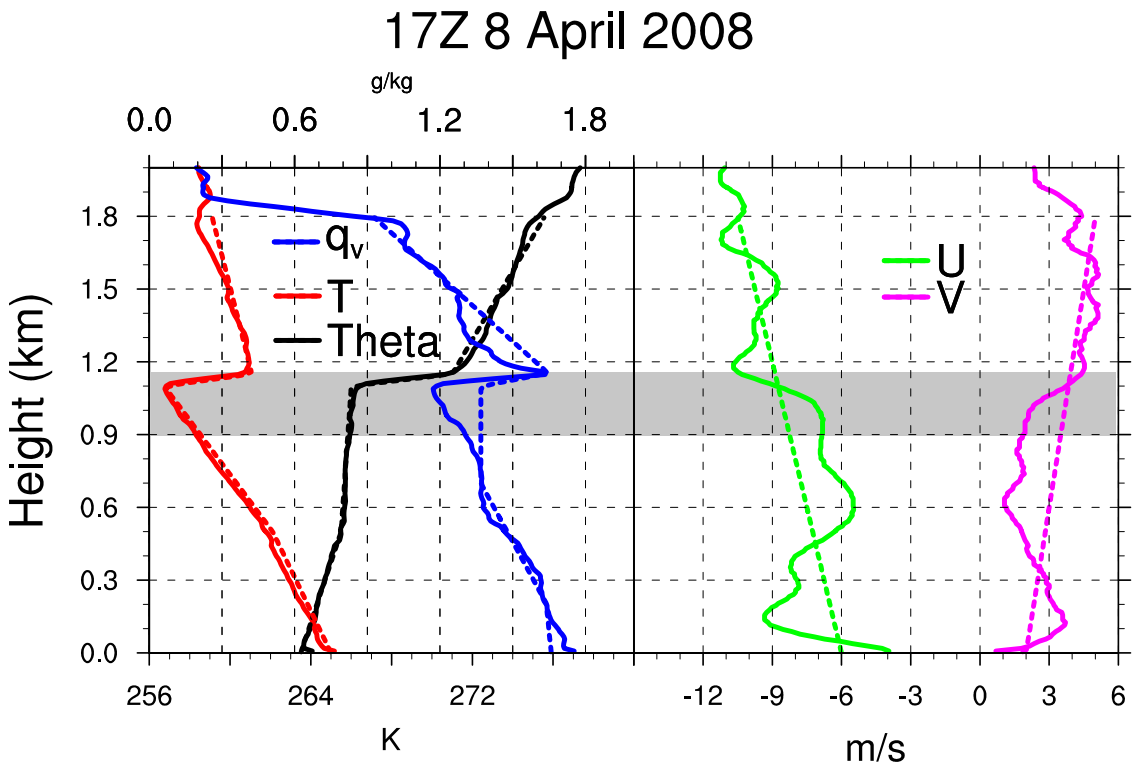

725 **Figure 1:** Sounding measured at 17:34 UTC 8 April 2008 at Barrow, Alaska (71.338N,
726 156.68W). Left) Water vapor mixing ratio (q_v), temperature (T), and potential temperature
727 (Theta), in units of g kg^{-1}, degrees Kelvin, and degrees Kelvin respectively. Right) Zonal
728 wind (U) and meridional wind (V), in units of m s^{-1}. Gray shading marks the extent of the
729 cloud layer. The dashed lines show the initial profiles used in the WRFLES experiments. The
730 dashed line overlaying water vapor mixing ratio is the initial profile for the total water
731 mixing ratio.

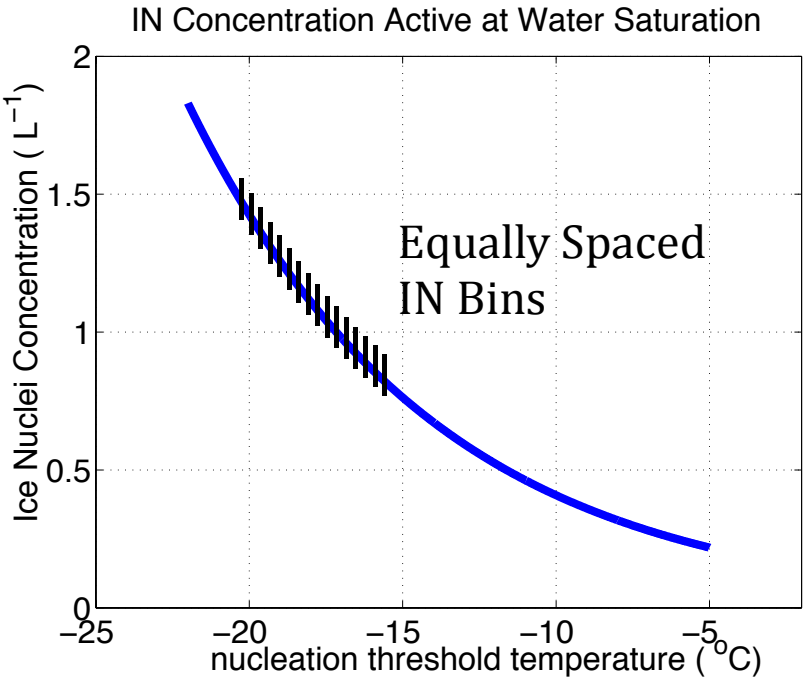

Figure 2: IN number concentration active at water saturation vs. temperature based on the empirical relationship derived in DeMott et al. (2010) (blue line) used to initialize IN number concentration in each bin. Black vertical lines indicate threshold temperatures for nucleation in the 16 IN bins. IN increments between lines indicate the additional IN available for nucleation at colder temperatures.

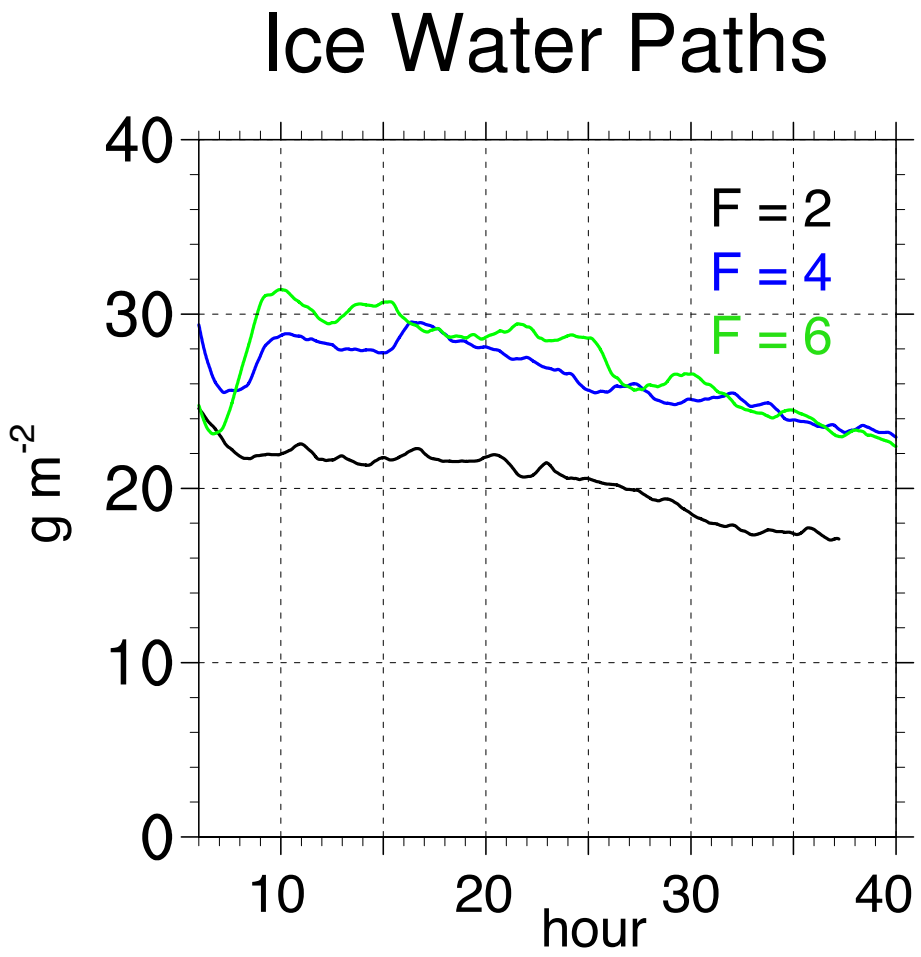

740

741 **Figure 3:** Sensitivity of ice water path to the parameter F in equation (2). Note the similar ice

742 water paths for F=4 and F=6 (total N_{IN} initial values of 5.8 and 8.7 L^{-1}, respectively).

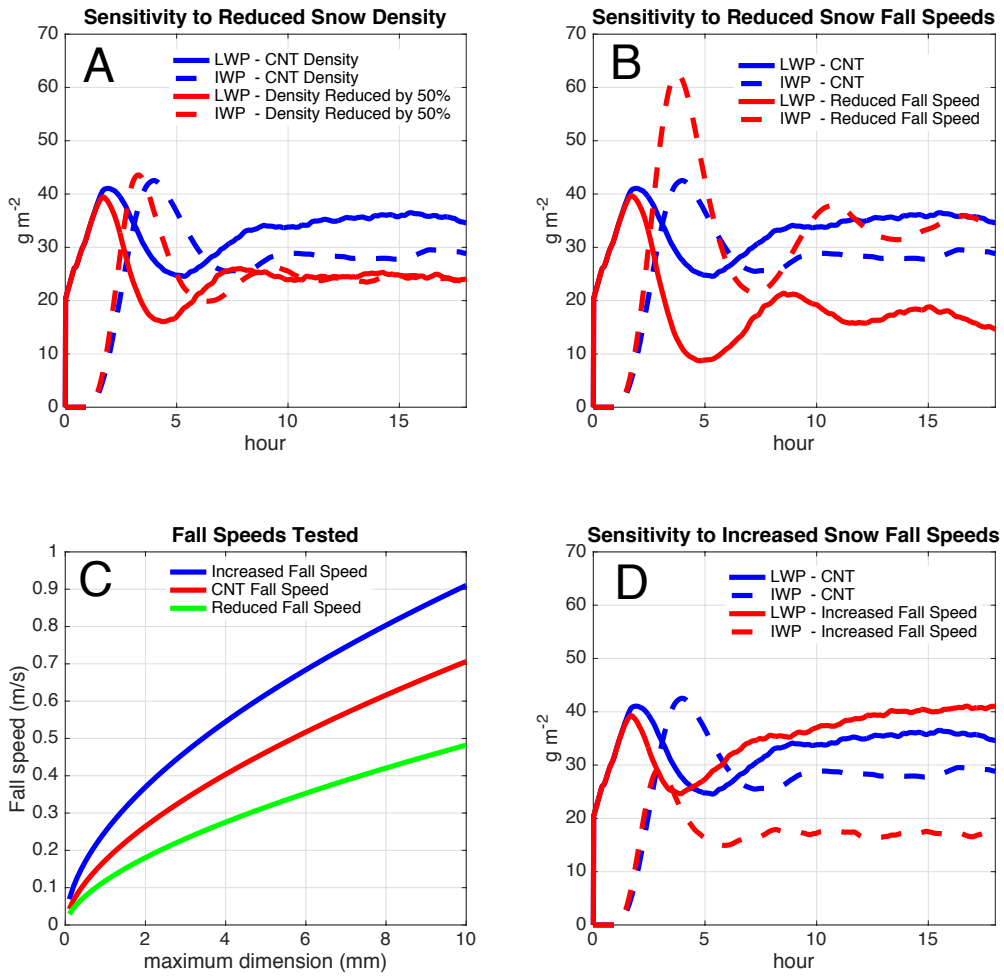

743

744 **Figure 4:** A,B,D) Sensitivity of LWP and IWP to snow density and fall speeds. LWP shown
745 with solid lines and IWP shown with dashed lines, in units of g m^{-2}. C) Fall speeds used in
746 sensitivity studies, in units of m s^{-1}. A) Sensitivity to reducing snow density from 100 kg m^{-3}
747 to 50 kg m^{-3} (red lines) using Control (CNT) fall speeds (red line in C). B) Sensitivity to
748 reducing snow fall speeds (green line in C) using Control snow density (red lines). D)
749 Sensitivity to increasing snow fall speeds (blue line in C) using Control snow density (red
750 lines).

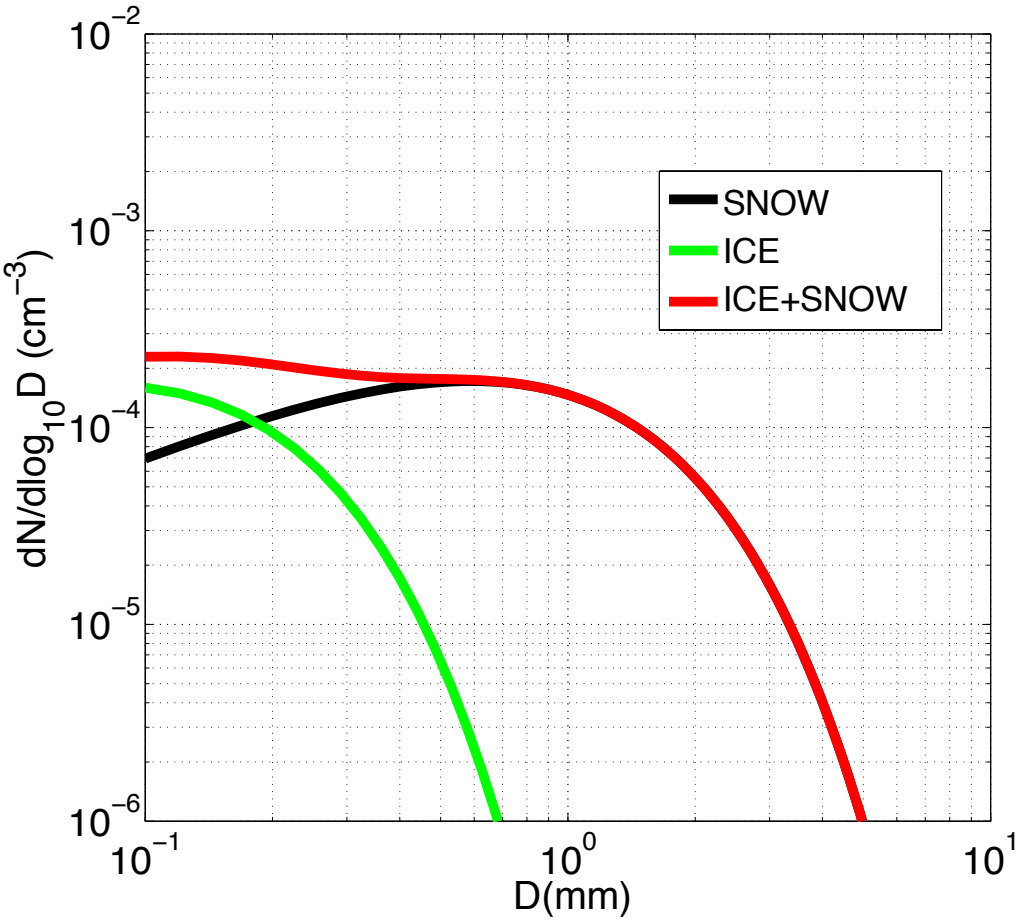

751

752 **Figure 5:** Simulated ice particle number size distributions using in-cloud mass and number

753 concentrations. Ice water mixing ratio = 3e-4 g/kg, ice number concentration = 0.4/L, snow

754 water mixing ratio = 2.4e-2 g/kg, snow number concentration = 0.45/L.

755

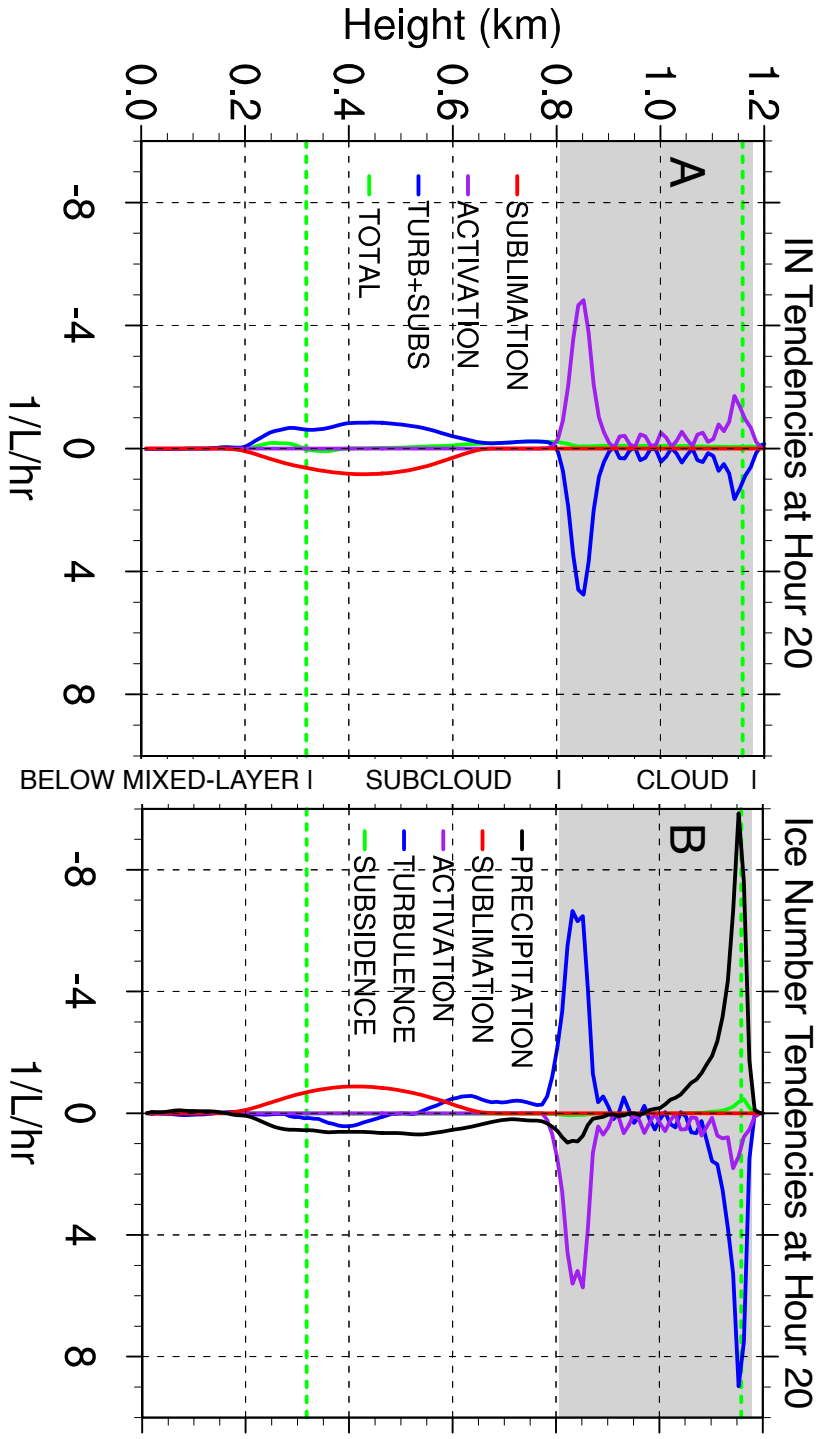

Figure 6: (A) N_{IN} and (B) N_{ICE} averaged over 0.5 hours at hour 20, in units of L^{-1} hr^{-1}. Grey shading indicates the extent of the cloud layer. Green dash lines indicate the top and bottom of the mixed layer.

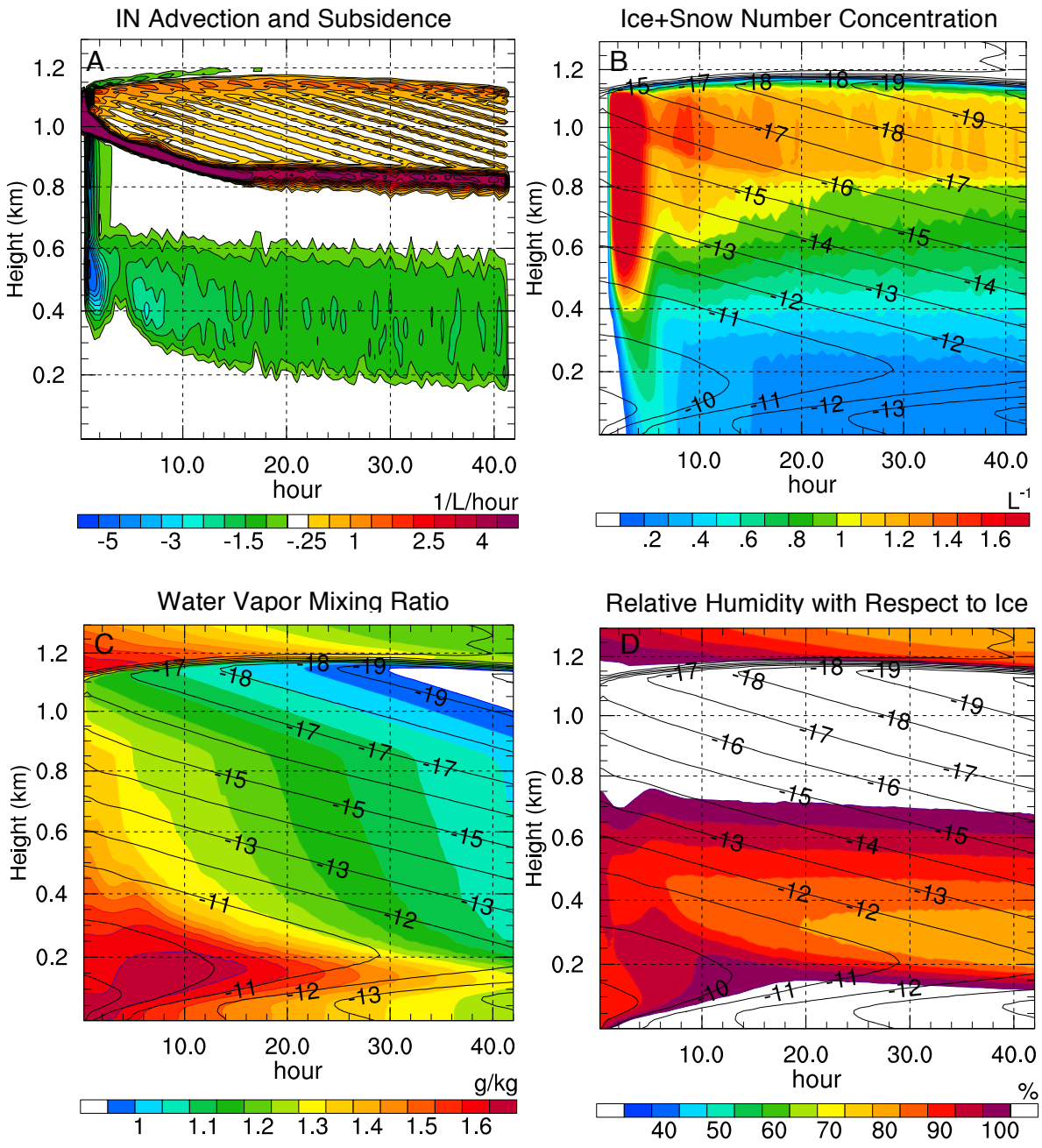

Figure 7: Time-height cross sections of horizontally-averaged (A) IN advection plus subsidence, in units of $L^{-1}hour^{-1}$, (B) ice plus snow number concentration, in units of L^{-1}, (C) water vapor mixing ratio, in units of g kg^{-1}, and (D) relative humidity with respect to ice, in units of percent, from CNT simulation. Temperature, in units of °C, shown with black contour lines in (B,C,D).

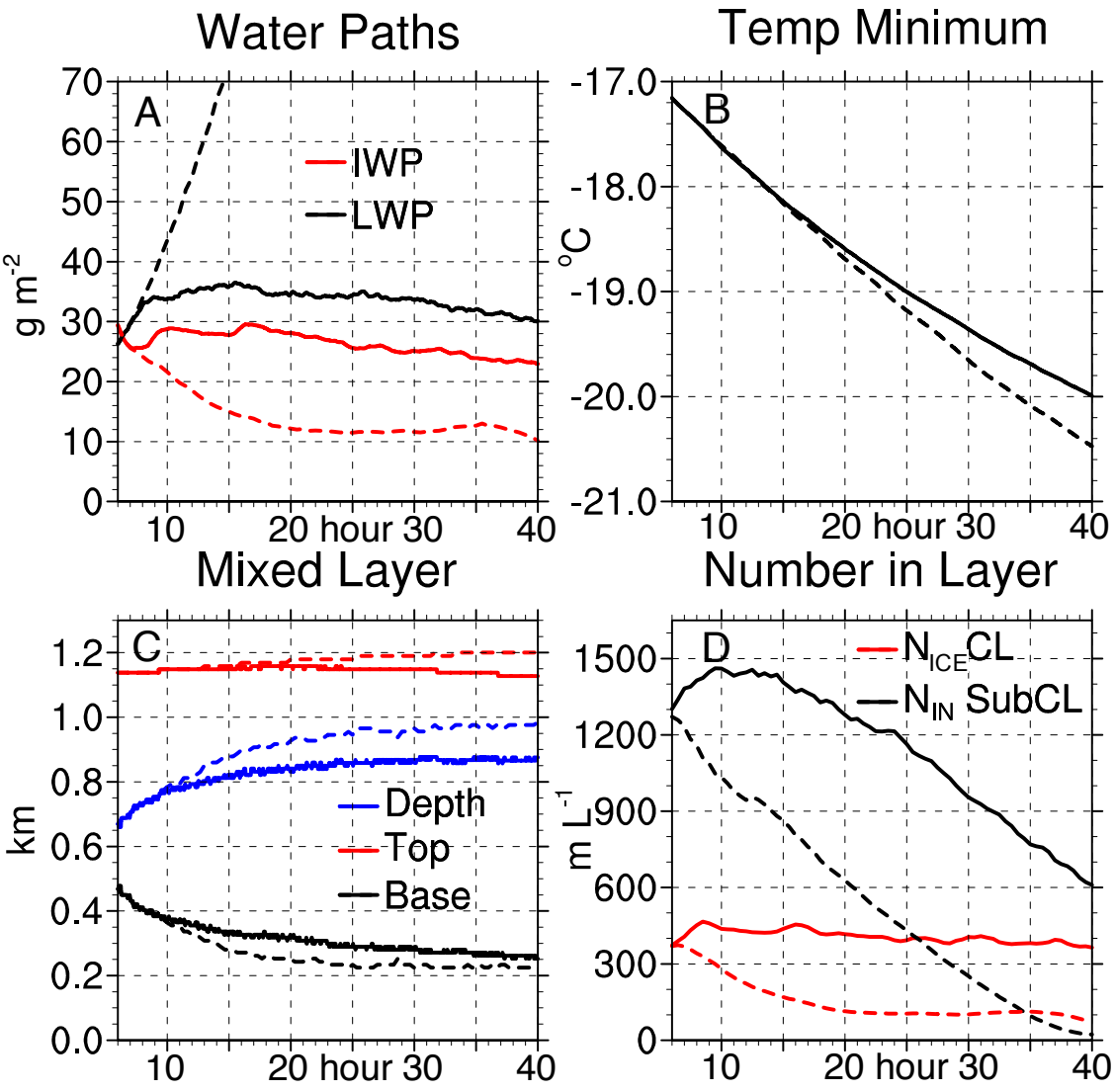

Figure 8: Control and NoRecycle time series for hours 6-40 (smoothed with 90 minute running average). NoRecycle shown with red and black dashed lines. A) LWP (black) and IWP (red), in units of g m^{-2}. B) Minimum horizontally-averaged temperature in the column, in units of ^{o}C. C) Mixed-layer depth (blue), top height (red), and base height (black), in units of km. D) N_{ICE} integrated over cloud layer (referred to as CL, red) and N_{IN} integrated over subcloud layer (referred to as SubCL, black), in units of m L^{-1}(i.e., meters/liter).

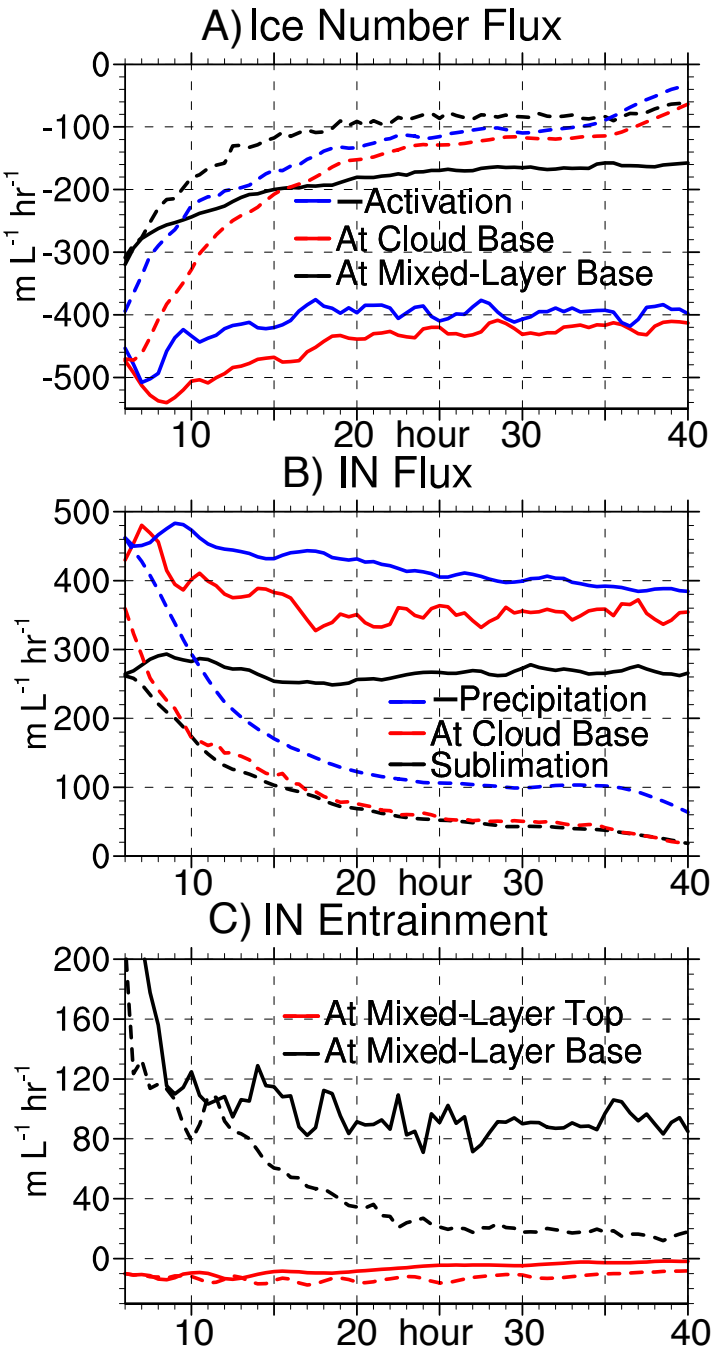

775

776 **Figure 9:** Horizontally-averaged fluxes from Control and NoRecycle integrations for hours
777 6-40 (smoothed with 90 minute running average). NoRecycle shown with dashed lines. A)
778 N_{NI} flux at cloud base due to turbulence+subsidence+precipitation (red), mixed-layer base
779 due to turbulence+subsidence+precipitation (black), and due to activation (multiplied by -1,
780 blue), in units of m L^{-1} hr^{-1}. B) N_{IN} flux at cloud base due to turbulence (red), N_{IN} flux due to
781 sublimation (black), and precipitation of N_{ICE} at cloud base (multiplied by -1, blue), in units
782 of m L^{-1} hr^{-1}. C) N_{IN} entrainment at mixed-layer top (red) and base (black), in units of m L^{-1}
783 hr^{-1}.

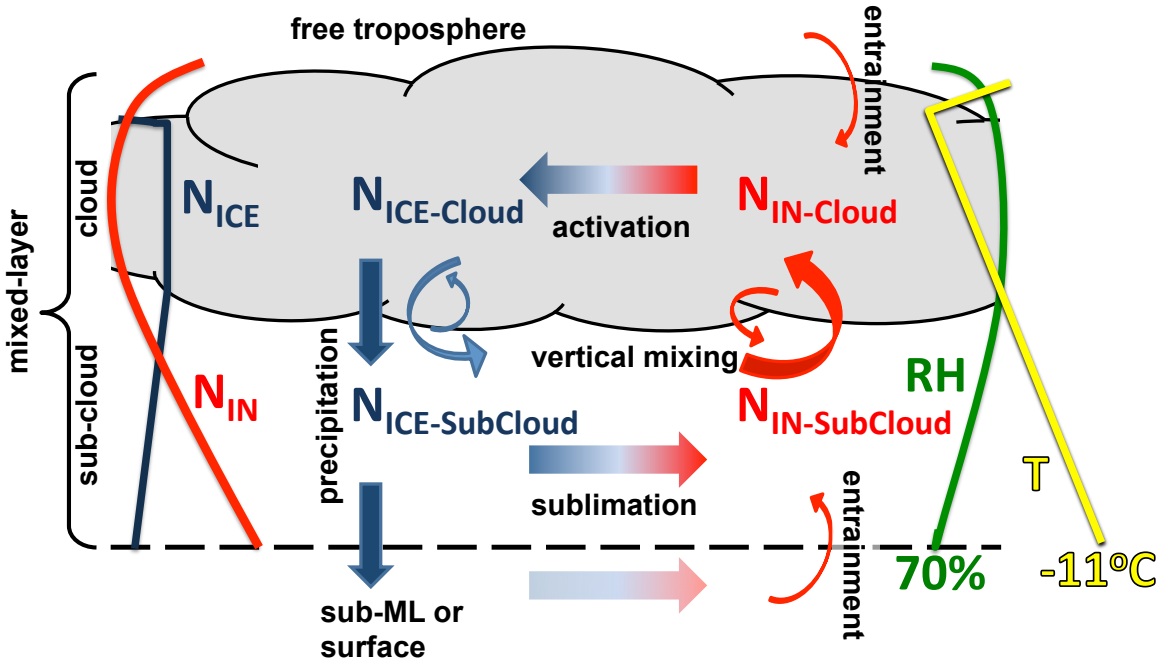

784

785 **Figure 10:** Schematic of feedback loops that maintain ice production and the phase-
786 partitioning between cloud liquid and ice in AMPS when recycling is allowed. Red colors
787 denote N_{IN}. Blue colors denote N_{ICE}. Vertical profiles of N_{ICE}, N_{IN}, relative humidity, and
788 temperature shown with thin blue, red, green, and yellow lines, respectively.

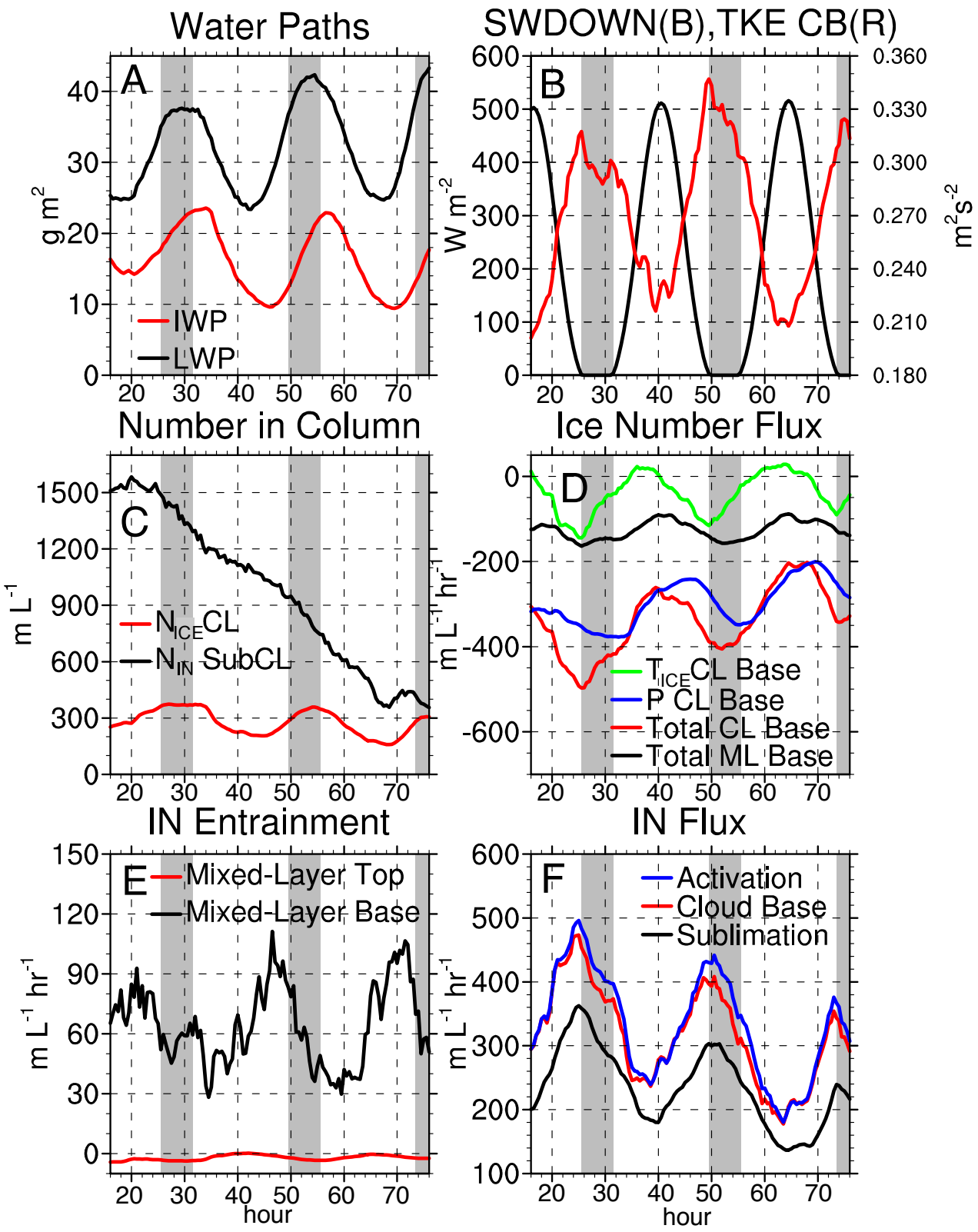

789

790 **Figure 11:** SW time series (see Figure captions).

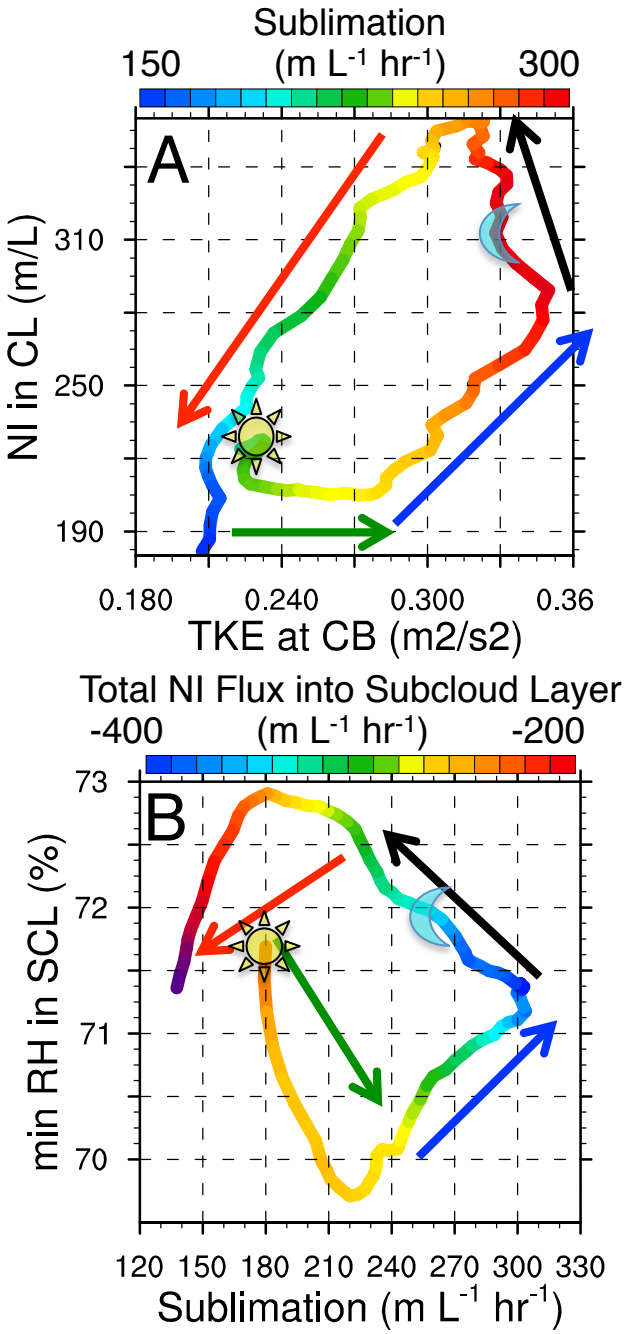

791

792 **Figure 12:** A) Phase diagram of TKE at cloud base vs. N_{ICE} in the cloud layer starting at
793 peak shortwave hour 40, in units of m L^{-1} and m L^{-1} hr^{-1}, respectively. Colors show
794 sublimation in units of m L^{-1} hr^{-1}. B) 24-hour phase diagrams of sublimation vs. minimum
795 relative humidity in the subcloud layer starting at peak shortwave hour 40, in units of m L^{-1}
796 hr^{-1} and %, respectively. Colors show total N_{ICE} flux at cloud base, m L^{-1} hr^{-1}. Hours 42-47,
797 47-50, 50-56, and 57-62 indicated with green, blue, black, red arrows, respectively.

798 Minimum shortwave indicated with the moon symbol. Maximum shortwave indicated with
799 the sun symbol.